AIAA JOURNAL
Vol. 34, No. 12, December 1996

Space-Time Correlation Measurements in a Hypersonic Transitional Boundary Layer

Roger L. Kimmel*
U.S. Air Force Wright Laboratory, Wright–Patterson Air Force Base, Ohio 45433-7913
Anthony Demetriades†
Montana State University, Bozeman, Montana 59717-0007
and
Joseph C. Donaldson‡
MicroCraft Technologies/Arnold Engineering Development Center, Arnold Air Force Base, Tennessee 37389-4001

An experimental investigation of the spatial structure of second-mode instability waves was carried out in the boundary layer of a 7-deg half-angle, sharp-nosed cone at an edge Mach number of 6.8. Measurements were made at Reynolds numbers of 2.3×10^6 to 9.1×10^6 based on boundary edge conditions, spanning the range from unstable laminar flow to nearly turbulent flow. Simultaneous measurements with two hot-film probes in the boundary layer comprise the primary data set. The mean boundary-layer state was measured with pitot and total temperature surveys. Correlations were taken with circumferential, streamwise, and vertical probe separations. Preliminary results show that the second-mode waves preceding transition are relatively limited in their circumferential dimension, typically less than four boundary-layer thicknesses, based on a coherence level of 20%. Streamwise convection velocities for the second mode are between 95 and 100% of the edge velocity, and wavelengths are approximately two boundary-layer thicknesses, in agreement with stability theory. The second-mode waves retain their identity well into the transition process. Structure angle measurements in the transitional boundary layer reveal that the second-mode waves are more highly inclined toward the wall than coherent structures typically observed in turbulent boundary layers.

Nomenclature

c_r	= convection velocity
f	= frequency
M_e	= boundary-layer edge Mach number
N	= number of time records averaged
Re_u	= freestream unit Reynolds number, m^{-1}
Re_{ue}	= boundary-layer edge unit Reynolds number, m^{-1}
S	= autopower spectrum
U_e	= boundary-layer edge velocity
x	= longitudinal distance from model apex to measuring station, measured along model centerline
y	= distance from model surface, measured perpendicular to model surface
y'	= y distance from model surface to point equidistant between two vertically separated probes
z	= distance along circular arc centered on model centerline
γ^2	= coherence function
δ	= boundary-layer thickness
θ	= structure angle; Fig. 8
θ_c	= cone half-angle
ξ_x, ξ_y, ξ_z	= probe separation in the x, y, z direction, respectively
σ	= rms
τ	= time delay, s
ϕ	= phase angle, deg

Presented as Paper 95-2292 at the AIAA 26th Fluid Dynamics Conference, San Diego, CA, June 19–22, 1995; received Oct. 6, 1995; revision received July 31, 1996; accepted for publication Aug. 19, 1996; also published in *AIAA Journal on Disc*, Volume 2, Number 1. This paper is declared a work of the U.S. Government and is not subject to copyright protection in the United States.

*Aerospace Engineer, WL/FIMA, 2645 Fifth Street, Suite 7. Senior Member AIAA.

†Professor, Mechanical Engineering Department. Associate Fellow AIAA.

‡Principal Engineer, Aerospace Systems Facility, 676 Second Street; currently Principal Engineer, Sverdrup Technology, Inc., Arnold Engineering Development Center Group.

Introduction

BOUNDARY-LAYER transition impacts hypersonic vehicle design through significant increases in heat transfer and skin friction that occur when the boundary layer transitions from laminar to turbulent flow. Hypersonic boundary-layer transition cannot yet be predicted accurately because of its complexity. Uncertainty in transition location leads to diminished vehicle performance, primarily because of the additional weight of thermal protection needed to accommodate heating uncertainty. These factors provide motivation for accurate transition prediction. Improved understanding of the physics of hypersonic transition will discern new phenomena and lead to more accurate transition predictions.

It has been recognized for many years that stability theory forms a foundation for the prediction of transition and the interpretation of experimental results.[1,2] However, very little experimental work has been carried out on hypersonic boundary-layer stability.[3–6] All of these cited measurements have been single-point, hot-wire measurements. To better understand the stability and transition process, however, multiple-point measurements that reveal parameters describing the spatial structure of instability waves, such as wavelength, convection velocity, and wave angle, are required. Recent computational efforts have recognized the importance of linear wave superposition and nonlinear wave interactions in the instability wave growth process and the breakdown process.[7–10] Spatial correlation measurements capable of resolving these wave processes in supersonic and hypersonic boundary layers have been rare. Some notable results include those of Owen and Horstman[11] at Mach 7.2, Demetriades and Laderman[12] at Mach 9.4, and Spina et al.[13] at Mach 3, all in turbulent boundary layers. Owen and Horstman[14] also measured space-time correlations using hot wires in the transitional hypersonic boundary layer on an axisymmetric ogive cylinder at a freestream Mach number of 7.4, but their spectral data do not show evidence of second-mode instabilities. It is possible that the second mode was present in their experiment but that their instrumentation did not have

sufficient frequency response to resolve it. The goal of this experiment was to measure space-time correlations in an $M_e = 6.8$ boundary layer to document the transition process from the regime of laminar flow, where linear instability waves are present, through the transition process, to turbulent flow. To the authors' knowledge, this experiment represents the first space-time correlations measured in a hypersonic transitional boundary layer where the transition process is clearly dominated by second-mode instability.

Experiment

Test Facility and Model

Arnold Engineering Development Center (AEDC) Tunnel B is a closed-circuit hypersonic wind tunnel with a 1.27-m-diam test section. Two axisymmetric contoured nozzles provide nominal Mach numbers of 6 and 8, and the tunnel may be operated continuously over a range of reservoir pressure levels from 689 to 6.21 MPa at Mach 8. A description of the tunnel can be found elsewhere.[15] Flowfield surveys were made using a retractable overhead drive mechanism. A remotely actuated shield protected the probes when not in use. An auxiliary onboard probe drive mechanism mounted on the model support sting was used to position a single probe in the model boundary layer at 0.895 m from the model apex. This mechanism traversed in the direction normal to the sting. No shield was provided for the probe mounted on this auxiliary drive.

The Tunnel B freestream mean and fluctuating flow has been extensively monitored and calibrated.[16] The mean Mach number on tunnel centerline is spatially uniform to within 1.2%. Broadband rms freestream mass flux fluctuations on centerline are 1.2–1.5% of local mean values, depending on tunnel unit Reynolds number. Broadband rms total temperature fluctuations are an order of magnitude smaller than mass flux fluctuations. The freestream disturbance spectrum peaks between 2 and 3 kHz and drops off above this as approximately $1/f$. The spectrum shape is similar for all unit Reynolds numbers for both mass flux and total temperature. At $Re_u = 1.64 \times 10^6$ m^{-1}, the rms mass flux fluctuations in the second-mode frequency band between 60 and 70 kHz are estimated to be 0.07%, based on integration of the spectrum. Modal diagrams[16] indicate a freestream disturbance source in addition to acoustic radiation from the tunnel sidewall boundary layers, perhaps total temperature nonuniformity due to uneven heating of the flow.

The basic model for the investigation was a 7-deg half-angle cone of 1.016-m length and 0.250-m base diameter, with interchangeable nose sections. A sharp nose was used that had a spherical radius of 3.8×10^{-5} m. To minimize any interference with the flow in the base region of the model caused by the presence of the onboard probe drive mechanism, a frustum was added to the basic cone model. This 7-deg frustum extended the model length to 1.283 m and had a base diameter of 0.315 m. The frustum had a narrow slot that accommodated the movement of the strut that supported the probe mounted on the onboard drive mechanism.

The model was instrumented with 20 pressure orifices. Eighteen pressure orifices were located on the 0-deg ray of the model, and two were located on the 180-deg ray. Two of these diametrically opposed orifices were connected in differential to a single transducer to assess model angle of attack, which was maintained at 0 deg within ± 0.1 deg. Four coaxial surface thermocouple gauges were located on the 90-deg ray. In addition, four thermocouples were installed on the inside surface of the model along the 95-deg ray to monitor the equilibration of the model shell temperature.

Detailed measurements of the boundary-layer stability characteristics of this model in Tunnel B at freestream Mach 8 are described elsewhere.[5,17,18] The boundary layer is unstable to first- and second-mode waves, with the second mode being dominant. Stetson and Kimmel[5] show that the second-mode waves occur as packets under these conditions. Computations detailing the eigenfunctions and most unstable wave angles for these modes are given elsewhere.[1,19] Parabolized stability equations (PSE) computations[10] indicate that the second-mode disturbance growth is linear to Reynolds numbers of 2.6×10^6.

Probe Instrumentation

Mean-flow boundary-layer measurements were made with pitot and total temperature probes. The outside diameter of the cylindrical pitot probe was 0.38 mm, and the inside diameter was 0.18 mm (0.038δ at $Re_u = 4.92 \times 10^6$ m^{-1}). The tip was telescoped in a succession of larger-diameter tubes for installation in the probe rake. The tube section adjacent to the probe orifice was bent to align the probe parallel to the model surface for the surveys. The unshielded total temperature probe was fabricated from a length of sheathed thermocouple wire (0.51 mm o.d.) with two 0.1-mm-diam wires. The wires were bared for a length of approximately 0.38 mm and a thermocouple junction of approximately 0.13 mm (0.027δ at $Re_u = 4.92 \times 10^6$ m^{-1}) diam was made.

The correlation measurements were carried out using custom-built hot-film probes and constant-current anemometers. The film anemometer probe designs followed the guidelines established elsewhere.[20] The probes consisted of a 100-mm-long, 2.7-mm-diam twin-bore alumina tube, sharpened at the front end and bearing twin 24-gauge (0.5-mm-diam) pure platinum leadwires in the bores. In one of two designs used, designated 70-series probes, the sharpened end terminated in a short length of 0.02-in.-diam quartz rod held parallel to the probe body. The film sensor was deposited at the tip of this quartz rod. In the other design used, designated 90-series, the platinum leadwires were stepped down to a diameter of 0.13 mm, and their ends were cemented with potter's glaze on the sharpened alumina tip; the sensor film then was applied across the tips of the two leadwires. In both designs the platinum sensor film was first painted on the quartz or glaze substrate using a liquid platinum resinate solution, and then fired at high temperatures to remove the liquid vehicle.

Typical thicknesses of films prepared in this manner were about 0.025 μm. The films were also about 0.5 mm long (in the direction parallel to the test surface and normal to the flow vector) and about 0.2 mm wide (in the direction normal to the test surface). Electrical resistance of such films typically ranged from 10 to 20Ω. For several months prior to their use in the experiment, the probes and their spares were subjected to periodic resistivity calibration in a controlled oven, to monitor their condition and measure their electrical properties. The probes have been found capable of enduring continuous exposure to temperatures of 870 K and dynamic pressures of order 140 kPa.

Flow fluctuation measurements were made using constant-current anemometry techniques. Three channels of constant-current anemometer electronics were used. One channel was based on the Philco-Ford ADP12/13 anemometer used in the earlier studies of boundary-layer stability at AEDC. Two channels were based on the VKF-91 pair of anemometers built by AEDC/VKF in 1991. The anemometer signal was recorded on a Bell and Howell model VR3700B FM magnetic tape recorder for subsequent analysis. In each channel the anemometer current control that supplies the heating current to the sensor is capable of maintaining the current at any one of 15 preset levels. The anemometer amplifier that amplifies the sensor response signal contains the circuits required to electronically compensate the signal for a 6-dB/octave rolloff that is characteristic of a hot-wire sensor. Unlike the frequency response of hot-wire anemometers, which theoretically depends only on the wire time constant, the response of film probes depends on two parameters: the film inherent time constant in the absence of the substrate, and the so-called loss factor, which combines film, flow, and substrate characteristics.[20] While the inherent time constant for the probes used in this test were estimated in the range 10–20 μs, the loss factors were higher than 100. Under such circumstances one can show[21] that the thermal-lag attenuation of the probes is 3-dB/octave, and the phase lag is 45-deg, over most of the frequency range of interest. Therefore, no differential phase lag between probes due to differences in the probe time constant or loss factor was expected in this experiment. On the other hand, some quantitative distortions of the flow fluctuation spectrum were expected, because the compensating amplifiers used had a gain of 6 dB/octave. However, these distortions were uniform for all probes and should have little effect on the measurement of correlation coefficients.

Signal analysis was performed using an HP3562-A digital signal analyzer. The HP3562-A samples at 256 kHz, and the FM tape was played back at one-eighth speed for analysis, giving an effective sample rate of 2.048 MHz. Data were low-pass filtered below 1.024 MHz to prevent aliasing. The HP3562-A performed software fast Fourier transforms on the data, which provided the basis for the

power and cross spectra. Statistical quantities were averaged over 120 records of 2048 points each for streamwise and circumferential probe spacings, and 60 records of 2048 points each for vertical separations. Tests with records of varying size indicated that 256 points per record provided adequate frequency resolution and statistical convergence. Histograms of phase angle indicated little jitter in the wave obliqueness.

The quantities of greatest interest in this study are the coherence and phase angle. Of these two, the phase angle is more prone to error. Some possible sources of significant phase error include differential phase lag in the anemometer and recording electronics, probe-to-probe differences in phase response, and phase differences incurred from inaccuracy in probe spatial positioning. Pretest calibration of the anemometers revealed that below 200 kHz, channel-to-channel phase differences were less than 2 deg. Because the thermal loss factors of the probes were relatively high, the probes could be expected to show a constant phase shift over the frequency band of interest, thus eliminating this factor as a significant error source. Error in the probe relative x and y spatial locations produces phase error due to the components of convection velocity in these directions. Assuming that disturbances convect at near the edge velocity (which is demonstrated in the Results section), phase error due to x-positioning error is approximately 3×10^{-4} deg per mm of misalignment per Hz. An estimated 0.1-mm uncertainty in the relative x location of two probes thus leads to an uncertainty of 6 deg in phase angle at 200 kHz. The error is proportionally less at lower frequencies. The error due to vertical displacement of the probes was estimated by measuring phase angle as one probe was held fixed at the maximum energy location, while the other probe was displaced relative to the other by ± 0.1 and ± 0.25 mm in the y direction, with a constant ξ_z separation of 9.5 mm. This y sensitivity arises from the eigenstructure of the second mode, i.e., the inclination of constant phase lines in the x–y plane. Results obtained for the second mode at a freestream unit Reynolds number of 3.28×10^6/m show a sensitivity of 43 deg per mm of y displacement. An estimated uncertainty of 0.03 mm in ξ_y thus produces an uncertainty of 1.3 deg in the second-mode phase at the maximum energy location in the boundary layer. This should be a worst case, because the change in phase with y is maximized at the second-mode frequency and at the maximum energy location.[22] The summation of these errors leads to a worst-case error of 9.3 deg.

The cross spectrum and the phase angle are subject to random errors due to the finite sample size used to estimate them. The cross-spectrum and phase-angle errors depend on the number of samples used to estimate them and the coherence of the two signals. Bendat and Piersol[23] give formulas for the standard deviation of cross spectrum and phase for normally distributed signals. The normalized rms error in the magnitude of the cross spectrum (the rms error in the magnitude divided by the magnitude) is equal to $1/(|\gamma|\sqrt{N})$. The rms error in the phase angle, in radians, is given as $(1 - \gamma^2)^{1/2}/(|\gamma|\sqrt{2N})$. Although the signals obtained in this study are not normally distributed, these estimates can be used to demonstrate the trend in rms phase error with coherence. For $N = 120$ records and $\gamma^2 = 0.9$, the rms phase error is 1.2 deg. For the same number of records and $\gamma^2 = 0.2$, the rms phase error increases to 7.4 deg.

Finally, no decomposition of the fluctuations into mass flux or total temperature was attempted in this measurement. According to linear stability theory the configuration of the disturbances is the same from one mode to the other. For example, the phase velocity and amplification rate should be the same for both density and total temperature fluctuations. The probe outputs were also linear combinations of these modes. For these reasons the correlations of the probe outputs should closely resemble the correlations of the flow fluctuation modes themselves. Hot-wire anemometry measurements of this same flowfield[5] in which the disturbances were separated into their mass flux and total temperature components showed identical amplification rates for both components.

Test Conditions

The experiment was conducted at a freestream Mach number of 7.93. The stagnation temperature was 728 K, and the cone wall condition was adiabatic. Tests were carried out at freestream (upstream of the model bow shock) unit Reynolds numbers of $Re_u = 1.64 \times 10^6$, 3.28×10^6, 3.94×10^6, 4.92×10^6, and 6.56×10^6/m by varying tunnel stagnation pressure. Measurements were carried out at a nominal x location 0.895 m aft of the model tip, producing local x-Reynolds numbers of 2.3×10^6, 4.6×10^6, 5.5×10^6, 6.8×10^6, and 9.1×10^6 based on the local boundary-layer edge unit Reynolds number and x distance.

One hot-film probe was mounted in the onboard drive at a fixed location $x = 0.895$ m. A rake containing up to four additional hot-film probes was mounted on the tunnel overhead drive. Measurements in the circumferential (or z) direction were carried out by positioning the probes at the maximum energy location in the boundary layer, holding the rake fixed, and rolling the model to drive the onboard probe away from the rake. The maximum energy location is defined here as the y location in the boundary layer at which the broadband rms signal from the hot-film probe is a maximum. Measurements were taken at increments of 3.18-mm circumferential separation, up to 63.5 mm between the onboard probe and the rake probe nearest it. Streamwise correlations were obtained by holding the onboard probe fixed with a circumferential separation of 6.35 mm from the nearest rake probe, and moving the rake downstream in increments of 3.18 mm, up to 25.4 mm downstream of the onboard probe. The onboard probe was held fixed at the maximum energy location, and the downstream probe was relocated at the maximum energy point at each downstream station.

The boundary-layer basic state was documented with surveys of mean pitot pressure and total temperature. During these surveys, two additional hot-film probes were mounted on the rake along with the pitot and total temperature probes. These additional hot-film probes were separated in the vertical (y) direction by 1.47 mm to obtain vertical correlations through the boundary layer.

Results

Mean-Flow and Power Spectra

Mean boundary-layer surveys are presented in Fig. 1. The boundary-layer profiles are laminar at $Re_u = 1.64 \times 10^6$, 3.28×10^6, and possibly 3.94×10^6/m. Profiles at $Re_u = 4.92 \times 10^6$ and 6.56×10^6/m are clearly transitional. Previous hot-wire studies[19] show that transition for this configuration, as defined by the x location where the second-mode amplitude reaches a maximum before decaying, begins at $x = 0.895$ m at $Re_u = 3.28 \times 10^6$/m, approximately. Heat transfer measurements reported elsewhere[24] show that the end of transition at $x = 0.895$/m, as defined by the peak in heat transfer, should occur at approximately $Re_u = 6.56 \times 10^6$/m.

Power spectra are presented in Fig. 2. The second mode is clearly apparent at each Reynolds number up to 6.56×10^6/m. The power spectra amplitudes are normalized by the broadband mean square of the signal. Previous work has shown that the peak second-mode frequency scales on the boundary-layer thickness and edge velocity[17] and is equal to approximately $U_e/2\delta$. This scaling occurs because the most amplified second-mode wavelengths tend to be approximately twice the boundary-layer thickness, and the second-mode phase

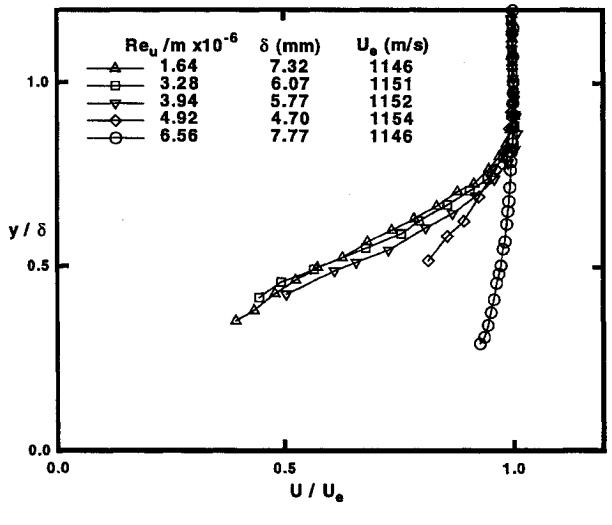

Fig. 1 Mean boundary-layer velocity profiles.

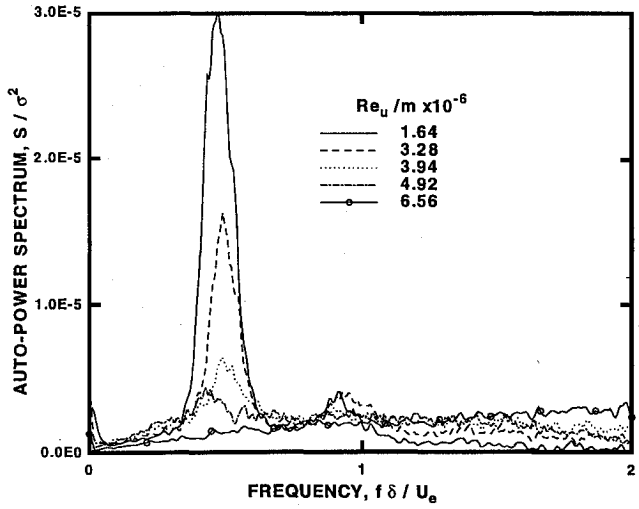

Fig. 2 Power spectra at maximum energy location.

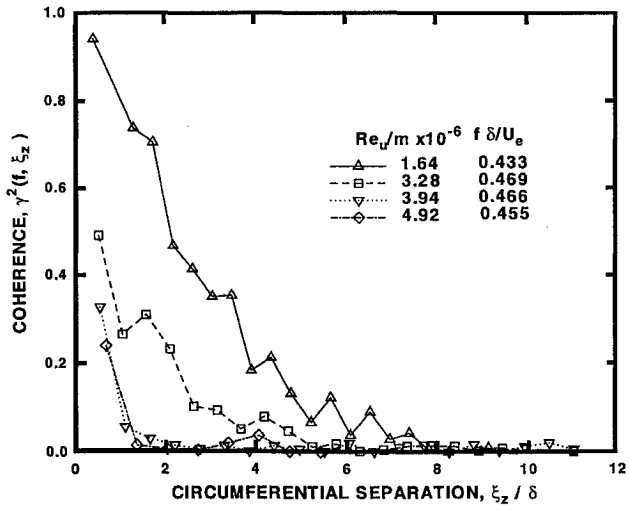

Fig. 4 Peak second-mode coherence vs circumferential separation.

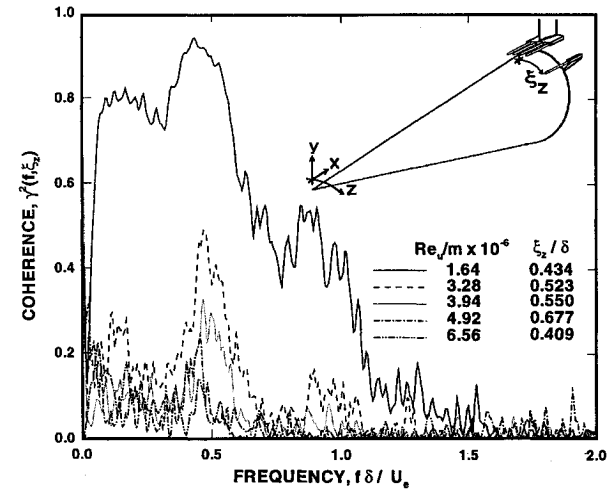

Fig. 3 Coherence function at minimum z separation.

velocities tend to be approximately equal to the edge velocity.[19] These ratios vary little with Reynolds number and frequency. Thus, when the power-spectrum frequency is scaled by U_e/δ, the second mode occurs at a nearly constant normalized frequency $f\delta/U_e$ of 0.5. Because of this property, the U_e/δ scaling is used here rather than the nondimensional frequency $2\pi f/U_e Re_{u_e}$ that typically is used in stability theory. A nonlinear harmonic[22] of the second mode occurs at a normalized frequency of approximately 1.0.

Measurements of amplification rates by Stetson et al.[17] on this configuration show that the second mode amplifies as Reynolds number increases, until transition occurs, and that the transition is clearly second-mode dominated. The raw anemometer signal at the second-mode frequency does increase with Reynolds number, but the contribution of the second mode to the overall signal rms decreases with Reynolds number, so that the normalized second-mode amplitude decreases with increasing Reynolds number. The spectra of Fig. 3 are in general agreement with spectra measured under similar conditions on the same model in the same wind tunnel, as reported elsewhere,[5,17] but have not been corrected for the probe frequency response. Therefore, Fig. 2 provides a qualitative guide to the spectral content of the signals, but cannot be considered quantitative.

Circumferential Probe Separation

The coherence as a function of frequency at minimum z separation is presented in Fig. 3. The minimum circumferential separation ξ_z is a constant 3.18 mm at each Reynolds number, but the normalized separation ξ_z/δ varies due to the change in boundary-layer thickness. The peak in the coherence at the second-mode frequency and harmonic is evident at each unit Reynolds number up to 6.56×10^6/m. At the lower unit Reynolds numbers, there is a notable coherence in the 0.1 to 0.2 range of normalized frequency, which is in the first-mode range.[19] Above unit Reynolds numbers of 1.64×10^6/m, there is little coherence at frequencies higher than the second mode except for the harmonic, indicating that disturbances at these frequencies have a predominant circumferential scale less than 3.18 mm.

In Fig. 4, the coherence function at the peak second-mode frequency is plotted as a function of circumferential separation. The peak second-mode frequency is defined here as the frequency at which the coherence is a maximum at $\xi_z = 3.18$ mm. Data at $Re_u = 6.56 \times 10^6$/m are not plotted because there is no clearly definable second mode at this Reynolds number. Figure 4 indicates that the circumferential scale of the second-mode wave packets, which tends to be 4δ or less, based on a coherence level of 20%, decreases with Reynolds number. The second-mode peak coherence at minimum spacing also decreases as unit Reynolds number increases, indicating that the circumferential scale of the second-mode wave packets decreases as the Reynolds number increases. Experiments in subsonic boundary layers have shown that the circumferential scale of wave packets grows as Reynolds number increases.[25] Because there is no evidence of breakdown at a freestream unit Reynolds number of 3.28×10^6/m, the decrease in circumferential scale may be due to a decrease in the scale of the freestream input disturbances. Because breakdown has begun at a unit Reynolds number of 3.94×10^6/m, as evidenced by previous studies,[17] the decrease in coherence at this Reynolds number may be due to some combination of breakdown and a decrease in input disturbance scale.

Streamwise Probe Separation

The convection velocity is the primary data of interest to be extracted from the cross spectrum for streamwise probe separation. The probes were separated in the circumferential as well as the streamwise direction to avoid interference between the upstream and downstream probes. Because the cross spectrum with circumferential separation showed that the waves are, on average, two dimensional, negligible error should be incurred because of the circumferential separation. The circumferential separation does create a problem at higher Reynolds numbers because of the drop in coherence with circumferential spacing. As noted in the discussion of statistical errors in the Experiment section, the uncertainty in cross-spectral quantities increases as the coherence decreases. Results for Reynolds numbers of 4.92×10^6 and 6.56×10^6/m are not presented because of the low coherence and noisy phase results. Because of the rapid dropoff in coherence in the z direction for the higher Reynolds numbers, meaningful convection velocities could not be extracted even using the broadband cross correlation. To obtain convection velocities at these Reynolds numbers, the probes would have to be spaced closer together in the z direction.

The convection velocity was extracted using the phase angle at the maximum streamwise separation of $\xi_x = 25.4$ mm for unit Reynolds numbers of 1.64×10^6 and 3.28×10^6/m. Using the maximum separation is desirable because the relatively large phase angle at this separation provides a good signal-to-noise ratio. Because of the overall low coherence at a unit Reynolds number of 3.94×10^6/m, the convection velocity is extracted using the minimum x separation, where coherence is highest. The streamwise convection velocity is defined as $c_r = \xi_x/\tau(f)$, where τ is the time delay between two signals. The time delay as a function of frequency is obtainable from the phase, because τ will be $\phi/360$th of a period, or $\tau = \phi(f)/360f$. Convection velocities are presented in Fig. 5. At unit Reynolds numbers of 1.64×10^6 and 3.28×10^6/m the normalized convection velocity c_r/U_e at the second-mode frequency is between 0.95 and 1.0, in agreement with Mack's[19] results for this configuration. The data scatter increases with unit Reynolds number and away from the second-mode frequency because of lower coherence. Data are not presented where the coherence is less than 0.05. At a unit Reynolds number of 1.64×10^6/m, the normalized convection velocity increases as frequency decreases, up to a level of about 1.1. The measured convection velocity of $0.984\,U_e$ at the second-mode frequency $f = 0.434\,U_e/\delta$ at unit Reynolds number 1.64×10^6/m indicates a wavelength of 2.3δ, which is in agreement with Mack's[19] computations.

Vertical Probe Separation

At a Reynolds number of 1.64×10^6/m, coherence measurements with vertical spacing of 1.47 mm (0.201δ) between probes (Fig. 6) show a maximum coherence above 0.6 in the second-mode range near the edge of the boundary layer. In principle, a second-mode wave should be coherent throughout the boundary layer. Away from the boundary-layer edge, however, the coherence for $\xi_y = 0.201\delta$ spacing is less than 0.2 because of the extremely low second-mode signal levels. The low coherence in the second-mode range above the boundary-layer edge indicates that any forcing input from the tunnel-wall boundary-layer noise is dwarfed in comparison to the second-mode signal.

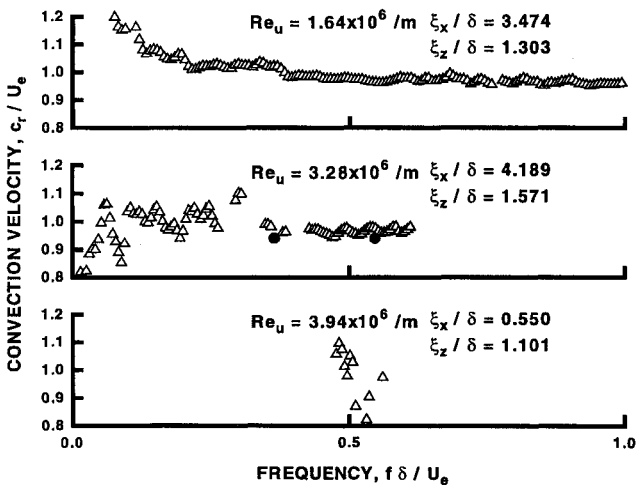

Fig. 5 Convection velocity as a function of frequency: solid circles at $Re_u = 3.28 \times 10^6$/m are computational results of Mack.[19]

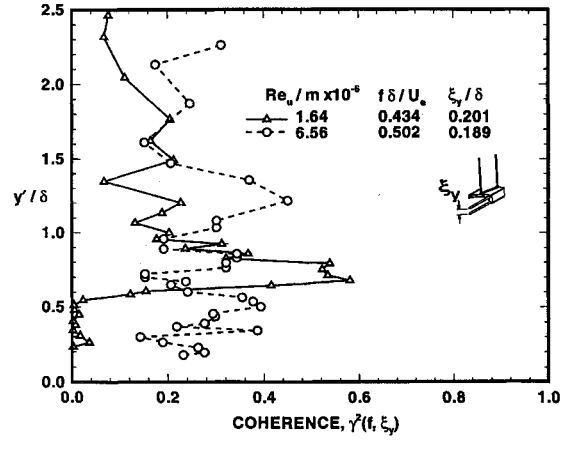

Fig. 6 Coherence for vertical probe separation through boundary layer.

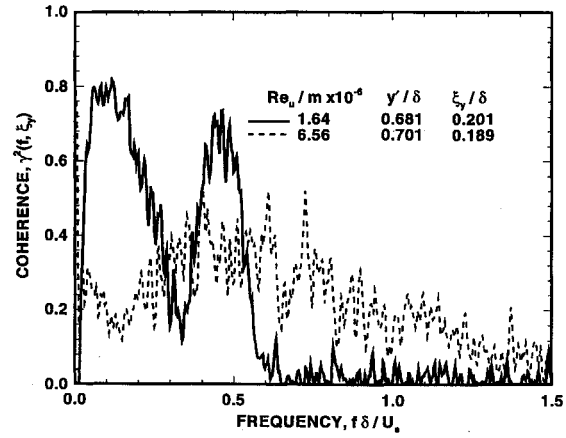

Fig. 7 Coherence for vertical probe for separation vs frequency near maximum energy location in boundary layer.

The maximum coherence (Fig. 6) within the boundary layer for probes separated vertically by 1.47 mm at a unit Reynolds number of 6.56×10^6/m, well into breakdown, is lower than the maximum coherence at $Re_u = 1.64 \times 10^6$/m, indicating that the vertical scale of disturbances has decreased because of the boundary-layer breakdown. However, the coherence in the interior of the boundary layer and above the boundary-layer edge is higher, indicating that this scale of disturbance is more uniformly distributed over the boundary layer. Power spectra taken at $Re_u = 6.56 \times 10^6$/m (Fig. 2) show that disturbance energy is distributed across a broader range of frequencies because of the boundary-layer breakdown. Coherence measurements near the maximum energy point in the boundary layer (Fig. 7) show that at a unit Reynolds number of 1.64×10^6/m, coherence on this scale is limited to the second mode and lower frequencies. At a unit Reynolds number of 6.56×10^6/m, the peak coherence is lower, but the high-frequency coherence increases, reflecting a coherent high-frequency component of the flow.

Phase information for vertically separated probes is typically presented as a "structure angle" θ for turbulent boundary layers. The structure angle is determined by the time delay between the top and bottom probes as $\theta = \tan^{-1}(\xi_y/c_r\tau)$, where τ is obtained from the cross-spectrum phase angle between the top and bottom probes. Structure angles must be interpreted differently for second-mode waves than for organized turbulent structures, because second-mode waves are periodic in the streamwise direction. Structure angles for second-mode waves represent the inclination of a line of constant phase in the x–y plane. Examination of this angle gives some indication of how the eigenstructure of the second-mode wave evolves into turbulent structures. Structure angles for all of the unit Reynolds numbers tested are shown in Fig. 8. Data are not presented where the coherence is less than 0.05. The angles for unit Reynolds numbers between 1.64×10^6 and 4.92×10^6/m, inclusive, are for the peak second-mode frequency. The angles for $Re_u = 6.56 \times 10^6$/m were obtained from the cross spectrum at $f\delta/U_e = 0.5$. Broadband results at this Reynolds number (not shown) are similar in shape, but about 8 deg higher. The convection velocity c_r was taken equal to $0.95U_e$. This is appropriate for the lower unit Reynolds numbers, but is probably an overestimate for $Re_u = 6.56 \times 10^6$/m. Other researchers[11–14] indicate normalized convection velocities between 0.8 and 1.0 for compressible turbulent and transitional boundary layers. A convection velocity of 0.8 would increase the measured wave angle by approximately 8 deg. The structure angles at $Re_u = 6.56 \times 10^6$/m show a relatively constant angle across the boundary layer of approximately 25–30 deg. This is in general agreement with the results of Owen and Horstman[11,14] for low-frequency disturbances in a hypersonic turbulent boundary layer

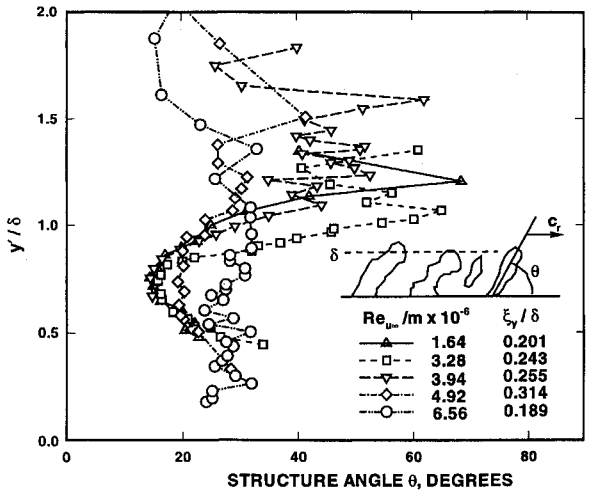

Fig. 8 Structure angle variation through boundary layer.

for $y/\delta \leq 0.6$. The present data, however, do not show the structure angle increasing with y, as Owen and Horstman[11,14] do, a trend that also was observed by Spina et al.[13] in a Mach 3 turbulent boundary layer. Structure angles are also generally less than observed by Spina et al.[13] These results indicate that the boundary layer has not relaxed to a fully turbulent structure at this Reynolds number.

The second-mode waves show a much different structure. Their structure angle within the boundary layer is generally less than the structure angle at 6.56×10^6/m unit Reynolds number. This structure angle decreases with y to a minimum of approximately 15 deg at $y/\delta = 0.7$. Above the boundary-layer edge, the inclination angle is higher at these Reynolds numbers compared to 6.56×10^6/m unit Reynolds number. This second-mode structure retains its identity through a unit Reynolds number of 4.92×10^6/m, although the change in structure angle begins to become evident. The structure angle changes abruptly as the boundary layer breaks down between 4.92×10^6 and 6.56×10^6/m.

Conclusions and Future Work

Space-time correlations in a transitional, $M_e = 6.8$ boundary layer have shown that the second-mode wave packets in this experiment have a limited circumferential extent, less than 4δ. First-mode disturbances have a similar circumferential extent. As freestream unit Reynolds number increases, the circumferential scale of the second-mode disturbances decreases. Part of this decrease in scale is probably due to a decrease in the scale of freestream turbulence that seeds the disturbances. At higher Reynolds numbers, this decrease in scale no doubt reflects the beginning of the breakdown process. Convection velocities for the second mode are between 0.95 and 1.0 U_e, which is within 5% of computational results. The second-mode streamwise wavelengths are approximately 2.3δ.

For two sensors with a fixed y separation that are traversed through the boundary layer, the coherence is a maximum near the boundary-layer edge at the second-mode frequency. For the same y separation, the maximum coherence decreases somewhat as the boundary layer breaks down. However, coherence in the interior of the boundary layer and at higher frequencies increases. This indicates that disturbances become less concentrated near the boundary-layer edge and are distributed more uniformly through the boundary layer and over the frequency spectrum. The second-mode waves retain their identity well into the breakdown process. The development of second-mode waves into a turbulent structure occurs relatively rapidly as the critical layer disappears and the second-mode wavefronts shift from a minimum orientation of approximately 15 deg into an orientation more typical of turbulent boundary layers.

This work represents a relatively preliminary study of second-mode wave structure and its evolution, and is based on ensemble-averaged cross spectra. Future work on these data will examine their time-dependent, nonstationary aspects, which will provide distributions of obliquity for second-mode wave packets and intermittency measurements for the developing turbulent boundary layer. These data, along with correlation measurements of the freestream turbulence spectrum, which will define the input disturbance field, will be used for detailed comparison with stability theory. Higher-order spectra, such as the bicoherence and cross bicoherence, are expected to shed light on the energy flow from the second mode to other wave numbers as the boundary layer breaks down.

References

[1]Mack, L. M., "Boundary-Layer Stability Theory," *Special Course on Stability and Transition of Laminar Flow*, edited by R. Michel, AGARD Rept. 709, 1984, pp. 3-1–3-81.

[2]Reshotko, E., "Stability Theory as a Guide to the Evaluation of Transition Data," *AIAA Journal*, Vol. 7, No. 6, 1969, pp. 1086–1091; also AIAA Paper 68-669, Jan. 1968.

[3]Kendall, J. M., "Wind Tunnel Experiments Relating to Supersonic and Hypersonic Boundary-Layer Transition," *AIAA Journal*, Vol. 13, No. 3, 1975, pp. 290–299; also AIAA Paper 74-133, Jan. 1974.

[4]Demetriades, A., "Hydrodynamic Stability and Transition to Turbulence in a Hypersonic Boundary Layer over a Sharp Cone," U.S. Air Force Office of Scientific Research, AFOSR TR-75-1435, Bolling AFB, DC, July 1975.

[5]Stetson, K. F., and Kimmel, R. L., "On Hypersonic Boundary-Layer Stability," AIAA Paper 92-0737, Jan. 1992.

[6]Lachowicz, J. T., Chokani, N., and Wilkinson, J. P., "Hypersonic Boundary Layer Stability over a Flared Cone in a Quiet Tunnel," AIAA Paper 96-0782, Jan. 1996.

[7]Pruett, C. D., and Zang, T. A., "Direct Numerical Simulation of Laminar Breakdown in High-Speed, Axisymmetric Boundary Layers," *Theoretical and Computational Fluid Dynamics*, Vol. 3, No. 6, 1992, pp. 345–367.

[8]Pruett, C. D., and Chang, C.-L., "Spatial Direct Numerical Simulation of High-Speed, Boundary-Layer Flows Part 2: Transition on a Cone in Mach 8 Flow," *Theoretical and Computational Fluid Dynamics*, Vol. 7, No. 5, 1995, pp. 397–424.

[9]Herbert, T., Stuckert, G. K., and Lin, N., "Method for Transition Prediction in High-Speed Boundary Layers," U.S. Air Force Wright Lab., Rept. WL-TR-93-3097, Wright–Patterson AFB, OH, Sept. 1993.

[10]Chang, C.-L., and Malik, M. R., "Non-Parallel Stability of Compressible Boundary Layers," AIAA Paper 93-2912, July 1993.

[11]Owen, F. K., and Horstman, C. C., "On the Structure of Hypersonic Turbulent Boundary Layers," *Journal of Fluid Mechanics*, Vol. 53, Pt. 4, 1972, pp. 611–636.

[12]Demetriades, A., and Laderman, A. J., "Space-Time Correlation Structure of Hypersonic Boundary Layers," *AIAA Journal*, Vol. 14, No. 2, 1976, pp. 256, 257.

[13]Spina, E. F., Donovan, J. F., and Smits, A. J., "On the Structure of High-Reynolds-Number Supersonic Turbulent Boundary Layers," *Journal of Fluid Mechanics*, Vol. 222, Jan. 1991, pp. 293–327.

[14]Owen, F. K., and Horstman, C. C., "Hypersonic Transitional Boundary Layers," *AIAA Journal*, Vol. 10, No. 6, 1972, pp. 769–775.

[15]Boudreau, A. H., "Performance and Operational Characteristics of AEDC/VKF Tunnels A, B, and C," Arnold Engineering Development Center, Rept. AEDC-TR-80-48 (AD A102614), Arnold AFB, TN, July 1981.

[16]Donaldson, J., and Coulter, S., "A Review of Free-Stream Flow Fluctuation and Steady-State Flow Quality Measurements in the AEDC/VKF Supersonic Tunnel A and Hypersonic Tunnel B," AIAA Paper 95-6137, April 1995.

[17]Stetson, K. F., Thompson, E. R., Donaldson, J. C., and Siler, L. G., "Laminar Boundary Layer Stability Experiments on a Cone at Mach 8, Part 1: Sharp Cone," AIAA Paper 83-1761, July 1983.

[18]Kimmel, R. L., and Kendall, J. M., "Nonlinear Disturbances in a Hypersonic Laminar Boundary Layer," AIAA Paper 91-0320, Jan. 1991.

[19]Mack, L. M., "Boundary-Layer Stability Analysis for Sharp Cones at Zero Angle-of-Attack," U.S. Air Force Wright Aeronautical Lab., Rept. AFWAL-TR-86-3022, Wright–Patterson AFB, OH, Aug. 1986.

[20]Demetriades, A., and Anders, S. G., "Characteristics of Hot Film Anemometers for Use in Hypersonic Flows," *AIAA Journal*, Vol. 28, No. 11, 1990, pp. 2003–2005.

[21]Demetriades, A., "Frequency Response of Constant-Current Film Anemometers," *International Journal of Heat and Mass Transfer*, Vol. 36, No. 1, 1993, pp. 231, 232.

[22]Malik, M. R., "Prediction and Control of Transition in Hypersonic Boundary Layers," AIAA Paper 87-1414, June 1987.

[23]Bendat, J. S., and Piersol, A. G., *Random Data Analysis and Measurement Procedures*, 2nd ed., Wiley, New York, 1986, pp. 294–302.

[24]Kimmel, R. L., "Experimental Transition Zone Lengths in Pressure Gradient in Hypersonic Flow," *Transitional and Turbulent Compressible Flows*, edited by L. D. Kral and T. A. Zang, ASME FED-Vol. 151, American Society of Mechanical Engineers, New York, 1993, pp. 117–128.

[25]Kendall, J. M., "Boundary Layer Receptivity to Freestream Turbulence," AIAA Paper 90-1504, June 1990.